AIAA Journal
Vol. 46, No. 4, April 2008

Large-Eddy/Reynolds-Averaged Navier–Stokes Simulation of a Mach 5 Compression-Corner Interaction

Jack R. Edwards,* Jung-Il Choi,† and John A. Boles‡
North Carolina State University, Raleigh, North Carolina 27695

DOI: 10.2514/1.32240

Simulations of Mach 5 turbulent flow over a 28-deg compression corner are performed using a hybrid large-eddy/Reynolds-averaged Navier–Stokes method. The model captures the mean-flow structure of the interaction reasonably well, with observed deficiencies relating to an underprediction of the displacement effects of the shock-induced separation region. The computational results provide some support for a recent theory concerning the underlying causes of low-frequency shock-wave oscillation. In the simulations, the sustained presence of a collection of streaks of fluid with lower/higher momentum than the average induces a low-frequency undulation of the separation front. Power spectra obtained at different streamwise stations are in good agreement with experimental results. Downstream of reattachment, the simulations capture a three-dimensional mean-flow structure, dominated by counter-rotating vortices that produce wide variations in the surface skin friction. Predictions of the structure of the reattaching boundary layer agree well with experimental pitot pressure measurements. In comparison with Reynolds-averaged model predictions, the hybrid large-eddy/Reynolds-averaged Navier–Stokes model predicts more amplification of the Reynolds stresses and a broadening of the Reynolds stress distribution within the boundary layer that is probably due to reattachment-shock motion.

Nomenclature

A = constant in the van Driest transformation
A_{sst} = turbulence model constant
a_1 = turbulence model constant
B = constant in the van Driest transformation
C = logarithmic-law wall intercept
C_f = skin friction
C_{Kleb} = constant in the Klebanoff intermittency function
C_p = specific heat at constant pressure (J/kg-K)
C_s = turbulence model constant
C_μ = turbulence model constant
d = distance to the nearest wall, m
d^+, d_w^+ = wall coordinates based on local kinematic viscosity
F_{kleb} = Klebanoff intermittency function
F_1, F_2 = blending functions
k = turbulence kinetic energy, $(\mathrm{m/s})^2$
M = Mach number
Pr_t = turbulent Prandtl number
p = pressure, $\mathrm{N/m^2}$
q = flow property
q' = flow-property fluctuation
R = gas constant, $\mathrm{J/kg \cdot K}$
Re = Reynolds number
r = wall recovery factor
S = strain rate, 1/s
T = temperature, K
t = time, s
u = velocity in the x direction, m/s
u_j = velocity component in coordinate direction j, m/s
u_{vd} = van Driest-transformed velocity, m/s
u_τ = friction velocity, m/s
v = velocity in the y direction, m/s
w = velocity in the z direction, m/s
X = distance along the surface, m
x_j = coordinate direction j, m
Y = distance normal to surface, m
Z = distance in the spanwise direction, m
α_1 = turbulence model constant
β = turbulence model constant
β^* = turbulence model constant
γ = turbulence model constant, ratio of specific heats, and intermittency
γ_R = probability of reversed flow
Δ = filter width, m
δ = boundary-layer thickness, m
δ^* = boundary-layer displacement thickness, m
η = ratio of turbulence length scales
θ = boundary-layer momentum thickness, m
κ = von Kármán constant
μ = molecular viscosity $\mathrm{kg/(m \cdot s)}$
μ_t = eddy viscosity, $\mathrm{kg/(m \cdot s)}$
ν = kinematic viscosity, $\mathrm{m^2/s}$
ν_t = kinematic eddy viscosity, $\mathrm{m^2/s}$
Π = wake parameter
ρ = density, $\mathrm{kg/m^3}$
σ_k = turbulence model constant
σ_ω = turbulence model constant
$\sigma_{\omega 2}$ = turbulence model constant
φ = turbulence model constants
χ = Taylor microscale, m
Ω = vorticity magnitude, 1/s
ω = turbulence frequency, 1/s

Subscripts

inflow = inflow
loc = local
min = minimum
max = maximum
Mork = Morkovin

Received 18 May 2007; revision received 31 October 2007; accepted for publication 13 November 2007.

*Professor, Department of Mechanical and Aerospace Engineering, Campus Box 7910; jredward@ncsu.edu. Associate Fellow AIAA.

†Research Assistant Professor, Department of Mechanical and Aerospace Engineering, Campus Box 7910; jchoi2@ncsu.edu.

‡Research Assistant, Department of Mechanical and Aerospace Engineering, Campus Box 7910; jaboles@ncsu.edu. Student Member AIAA.

o = stagnation conditions
prov = provisional
recyc = recycle plane
t = turbulent
w = wall
x, y, z = Cartesian coordinates
0 = reference condition for boundary-layer thickness
∞ = freestream

Superscripts

$'$ = fluctuation
$''$ = fluctuation

I. Introduction

THE accurate prediction of high-speed flows can depend critically on the ability of the chosen model to account for shock-wave/boundary-layer interactions. For example, off-design aerodynamic performance of missiles can be affected by shock/boundary-layer interactions induced by plume interference, and the initial stages of launch for many ballistics concepts involve multiple shock/boundary-layer interactions. Maneuvering of launched missiles may involve movement of fins or control surfaces, which could also result in shock/boundary-layer interactions. A clear understanding of the effects of the associated fluctuating pressure and heating loads is necessary to better refine control techniques, to predict failure scenarios, and to determine ranges of efficient operation. A complicating factor in many shock-wave/boundary-layer interactions is a degree of global flowfield unsteadiness, apart from that due to turbulent fluctuations, that can dominate the response. The work of Dolling and his colleagues [1–11], spanning over 20 years, has provided the most complete characterization of the dynamics of shock/boundary-layer interactions. The database includes conditionally averaged pitot and static pressure distributions (conditioned on the separation-shock position); wavelength, amplitude, and frequency information associated with the shock structure; and cross-correlation analyses designed to elucidate the underlying causes of the global motion. Trends revealed during this study raise serious concerns about the ability of traditional Reynolds-averaging techniques to predict shock/boundary-layer interactions and appear to indicate that time-accurate, three-dimensional modeling strategies [such as direct numerical simulation (DNS) or large-eddy simulation (LES)] may be required for precision. Early LES and DNS studies of shock/boundary-layer interactions [12–15] were conducted at Reynolds numbers substantially lower than most experimental databases and therefore emphasized only qualitative comparisons with experimental data. These fundamental studies are now being supplemented with quantitative investigations that attempt one-to-one comparisons with experimental data at the same flow conditions [16,17], and the present work falls within this scope.

The objective of the current work is to apply a hybrid LES/RANS framework [18–22] developed at North Carolina State University (NCSU) to the Dolling Mach 5 compression-corner configuration [5,6] to determine the model's ability to capture the time-dependent structure of this flow. The viewpoint taken in the NCSU model is that the RANS component functions as a form of near-wall closure in an otherwise LES description of the flow. A strong coupling of the model response with the boundary-layer structure is therefore required, and this is facilitated first by the design of a RANS-to-LES-transition function that is based on the modeled structure of the flow in the logarithmic region, and second, by the use of "recycling/rescaling" techniques that sustain the transport of large turbulent structures in the outer part of the boundary layer. Although predictions of mean-flow properties have been evaluated in earlier works [18–22], this study also focuses on the prediction of second-moment quantities and on the dynamics of the shock/boundary-layer interaction. In this, the present work is closely related to the Mach 3 LES investigation of flow over a compression corner conducted by Loginov et al. [16], the Mach 3 DNS compression-corner calculations of Wu and Martin [17], and the earlier "very" large-eddy simulations of Mach 3 flow over a compression corner of Hunt and Nixon [23]. Both the Loginov et al. [16] and Wu and Martin [17] investigations used over 18 million mesh points in their calculations. Because of the near-wall modeling in our hybrid LES/RANS approach, we can reduce the resolution requirements significantly and can compute flows at even higher Reynolds numbers. It will be shown that many of the features of the Dolling-group compression-corner experiments [5,6] are captured to a good degree of precision by the hybrid LES/RANS model. The remainder of this report outlines the numerical methods used (Sec. II), the turbulence closure models (Sec. III), and other calculation details (Sec. IV). The results of the investigation are presented in Sec. V, and some conclusions are outlined in Sec. VI.

II. Numerical Methods

Simulations were performed using NCSU's REACTMB code [24]. In REACTMB, the governing equations are discretized in a finite volume manner. Inviscid fluxes are discretized using Edwards's [25] low-diffusion flux-splitting scheme (LDFSS) scheme, whereas viscous and diffusive fluxes are discretized using second-order central differences. The LDFSS scheme is extended to second- or higher-order spatial accuracy using the piecewise parabolic method (PPM) [26]. The PPM reduces to a fourth-order central-differencing scheme for sufficiently smooth data, enhancing its ability to capture high-frequency features. The PPM requires a seven-point stencil in each coordinate direction, and the reconstruction procedures are applied to the primitive-variable vector $\boldsymbol{V} = [\rho, u, v, w, T, k, \omega]^T$. A dual-time-stepping implicit method is used to advance the equations in time. At each time step, a Crank–Nicholson discretization of the equations is solved to a prescribed tolerance using a subiteration procedure. The matrix system resulting from the linearization of the equation system is approximately solved using a planar relaxation procedure at each subiteration. To enhance computational efficiency, matrix elements are evaluated and factored every second time step and are held fixed over the duration of the subiterations.

III. Turbulence Closure

A. Menter's SST Model

The RANS turbulence model used in this investigation is Menter's hybrid k-ω/k-ε shear stress transport (SST) model [27]. The transport equations for the turbulence kinetic energy k and the specific dissipation rate ω for Menter's model are given by

$$\frac{\partial(\rho k)}{\partial t} + \frac{\partial(\rho k u_j)}{\partial x_j} = \mu_t S^2 - \beta^* \rho \omega k + \frac{\partial}{\partial x_j}\left[(\mu + \sigma_k \mu_t)\frac{\partial k}{\partial x_j}\right] \quad (1)$$

$$\frac{\partial(\rho \omega)}{\partial t} + \frac{\partial(\rho \omega u_j)}{\partial x_j} = \gamma \rho S^2 - \beta \rho \omega^2 + \frac{\partial}{\partial x_j}\left[(\mu + \sigma_\omega \mu_t)\frac{\partial \omega}{\partial x_j}\right] + 2(1 - F_1)\rho \sigma_{\omega 2}\frac{1}{\omega}\frac{\partial k}{\partial x_j}\frac{\partial \omega}{\partial x_j} \quad (2)$$

where S is defined as

$$S = \left[\frac{\partial u_i}{\partial x_j}\frac{\partial u_j}{\partial x_i} + \frac{\partial u_i}{\partial x_j}\frac{\partial u_i}{\partial x_j} - \frac{2}{3}\left(\frac{\partial u_i}{\partial x_i}\right)^2\right]^{1/2} \quad (3)$$

Values for the constants σ_k, σ_ω, β^*, β, γ, and $\sigma_{\omega 2}$ and the blending function F_1 may be found in [27]. The eddy viscosity is defined as

$$\mu_t = \rho \nu_t = \frac{a_1 k}{\max(a_1 \omega, A_{\mathrm{sst}} \Omega F_2)} \quad (4)$$

where $a_1 = 0.31$, Ω is the magnitude of the vorticity vector, and F_2 is another blending function given by

$$F_2 = \tanh\left(\mathrm{arg}_2^2\right), \qquad \mathrm{arg}_2 = \max\left(2\frac{\sqrt{k}}{0.09\omega d}, \frac{500\nu}{d^2\omega}\right) \tag{5}$$

where d is the distance to the nearest wall, and ν is the kinematic viscosity. This SST modification alters the turbulence frequency as used in the eddy viscosity definition in the vicinity of high strain rates. The general effect is to lower the eddy viscosity and thus to promote the growth of regions of separated flow. As shown later, the RANS predictions for Dolling's compression-corner experiments [5,6] (and similar shock/boundary-layer interactions) are sensitive to the constant A_{sst} in Eq. (4), which ranges between zero (for no SST modification) to one (for the full SST contribution).

B. Hybrid LES/RANS Extension

Several approaches were used in our earlier work to extend Menter's model to serve as the RANS component of a hybrid LES/RANS closure [18–22]. In this investigation, we have opted for a simple strategy motivated by Strelets's [28] development of a two-equation detached-eddy simulation method. The eddy viscosity as used in the turbulence transport equations and the main flow equations is defined as a weighted sum of a RANS description and a Smagorinsky model:

$$\mu_t = \rho\nu_t = \rho\left(\Gamma\frac{a_1 k}{\max(a_1\omega, A_{\mathrm{sst}}\Omega F_2)} + (1-\Gamma)C_s\Delta^2 S\right)$$
$$\Delta = (\Delta_x\Delta_y\Delta_z)^{1/3}, \qquad C_s = 0.01 \tag{6}$$

The blending function Γ is designed to shift the closure from a RANS description near solid surfaces to an LES description in the outer parts of the boundary layer and in regions of flow separation. The blending function is based on the ratio of the wall distance d to a modeled form of the Taylor microscale:

$$\Gamma = \frac{1}{2}\left(1 - \tanh\left[5\left(\frac{\kappa}{\sqrt{C_\mu}}\eta^2 - 1\right) - \phi\right]\right), \qquad \eta = \frac{d}{\alpha_1\chi} \tag{7}$$

with the Taylor microscale defined as

$$\chi = \sqrt{\nu/C_\mu\omega} \tag{8}$$

The primary advantage of this form is that the location of the RANS/LES juncture (defined as $\Gamma = 0.5$) can be correlated as a function of the wall coordinate $d^+ = u_\tau d/\nu$. Substituting the log-law expression for the turbulence frequency $\omega = u_\tau/(\sqrt{\beta_*}\kappa d)$ into Eq. (8) and placing the result in Eq. (7), it can be shown that the $\Gamma = 0.5$ position should occur at $d^+ = \alpha_1^2$ if $\phi = 0.0$. The constant α_1 then can be used control the position of the juncture, assuming that the log-law scaling is maintained. The value of 5 in Eq. (7) controls the sharpness of the transition, and the constant ϕ can be used to shift the midpoint of the blending function. In this work, ϕ is set to 2.2975599, so that the balancing position [where $(\kappa/\sqrt{C_\mu})\eta^2 = 1$] corresponds to $\Gamma = 0.99$ instead of $\Gamma = 0.5$.

To determine the constant α_1 for a particular inflow boundary layer, the following procedure is used. First, a prediction of the equilibrium boundary layer is obtained, given freestream properties, a specified wall condition (adiabatic or isothermal), and a value for the boundary-layer thickness (0.0175 m for the Mach 5 experiments) from Coles's law of the wall/wake, along with the van Driest transformation:

$$\frac{u_{\mathrm{vd}}}{u_\tau} = \frac{1}{\kappa}\ln(d_w^+) + C + 2\frac{\Pi}{\kappa}\sin^2\left(\frac{\pi}{2}\frac{d}{\delta}\right), \qquad d_w^+ = \frac{u_\tau d}{\nu_w} \tag{9}$$

with

$$u_{\mathrm{vd}} = \frac{u_\infty}{A}\left\{\sin^{-1}\left[\frac{2A^2 u/u_\infty - B}{\sqrt{B^2+4A^2}}\right] + \sin^{-1}\left[\frac{B}{\sqrt{B^2+4A^2}}\right]\right\}$$
$$A = \sqrt{\frac{(\gamma-1)}{2}\mathrm{Pr}_t M_\infty^2\frac{T_\infty}{T_w}} \tag{10}$$
$$B = \left[1 + \mathrm{Pr}_t^{1/2}\frac{(\gamma-1)}{2}M_\infty^2\right]\frac{T_\infty}{T_w} - 1$$

An initial estimate for the outer extent of the log layer is defined by finding the value of d_w^+ such that

$$\frac{(1/\kappa)\ln(d_w^+) + C}{u_{\mathrm{vd}}/u_\tau} = 0.98 \tag{11}$$

The value of $d^+ = u_\tau d/\nu$ that corresponds to this value of d_w^+ is then found through the use of Walz's [29] formula for the static temperature distribution within the boundary layer:

$$\frac{T}{T_\infty} = \frac{T_w}{T_\infty} + \frac{(T_{aw} - T_w)}{T_\infty}\frac{u}{u_\infty} - r\frac{(\gamma-1)}{2}M_\infty^2\left(\frac{u}{u_\infty}\right)^2 \tag{12}$$

Because the kinematic viscosity ν is a function of temperature, the target value for d^+ will differ significantly from d_w^+ for high Mach number flows. For the inflow boundary layer in the Mach 5 experiment, a value of $\alpha_1 = 42.042$ is calculated using this procedure.

A key to the blending-function response is the relative insensitivity of the turbulence frequency to changes in the turbulence kinetic energy and the eddy viscosity. This means that the average location of the blending function (in terms of its distance from the wall) will not vary significantly as the model shifts from RANS to LES. The dependence of the turbulence frequency on the local strain rate S means that the instantaneous position of the interface will vary in response to resolved-eddy dynamics. The preceding calibration procedure is specific to a particular inflow boundary layer, and it is not completely clear that the procedure is self-similar, in that the $\Gamma = 0.5$ blending-function position would recover to its target location if the initial equilibrium boundary layer relaxes to another equilibrium state. One way to examine similarity without the expense of a full hybrid LES/RANS calculation is to use a RANS mean-flow solution (obtained using $A_{\mathrm{sst}} = 0.87$ for reasons discussed later) to provide the basic state for the evolution of the hybrid turbulence model [Eqs. (1) and (2), closed by Eqs. (6) and (7)]. Figure 1 presents the blending function Γ and the van Driest-transformed velocity versus the wall coordinate d_w^+ for several axial stations upstream and downstream of the compression-corner configuration (described in

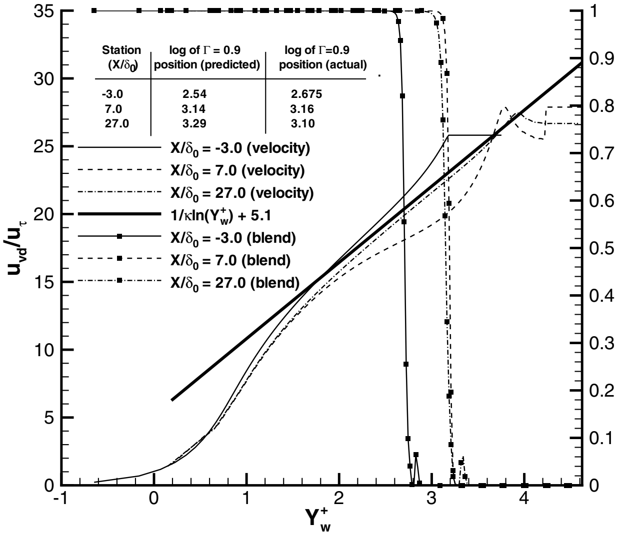

Station (X/δ_0)	log of $\Gamma = 0.9$ position (predicted)	log of Γ=0.9 position (actual)
-3.0	2.54	2.675
7.0	3.14	3.16
27.0	3.29	3.10

Fig. 1 Predictions of blending-function position at different X stations (RANS mean flow).

Sec. IV.A). The end-of-ramp portion is extended from $\sim 7X/\delta_0$ to $\sim 30X/\delta_0$ to allow the computed boundary layer to return nearly to equilibrium. Figure 1 shows that the actual $\Gamma = 0.5$ positions (in wall coordinates) are close to those predicted from the equilibrium analysis at all stations. This analysis, however, does not consider the effects of unsteady strain rates and thus may not be completely representative of the model response in an actual hybrid LES/RANS calculation.

C. Recycling/Rescaling Method

A recycling/rescaling technique applied to the fluctuating fields is used to initiate and sustain turbulent structures. In this procedure, fluctuations in the fluid properties at a "recycle plane" are extracted by subtracting the instantaneous profile from a time- and span-averaged profile. The fluctuation fields are then rescaled according to boundary-layer similarity laws and superimposed onto a RANS mean-inflow profile. The general procedure is described in [19,20]. One modification used in this work to prevent excessive turbulence energy accumulation in the outer part of the boundary layer is to multiply the recycled fluctuations by a Klebanoff-type intermittency function [30]:

$$
\begin{aligned}
q_{\mathrm{inflow}} &= q_{\mathrm{RANS}} + F_{\mathrm{Kleb}} q'_{\mathrm{recyc}} \qquad q = \rho, T, u_j \\
q_{\mathrm{inflow}} &= (1 - F_{\mathrm{Kleb}}) q_{\mathrm{RANS}} + F_{\mathrm{Kleb}} q_{\mathrm{recyc}} \qquad q = k, \omega, \Gamma \\
F_{\mathrm{Kleb}} &= (1 + (d/C_{\mathrm{Kleb}}\delta)^6)^{-1}
\end{aligned}
\tag{13}
$$

with $C_{\mathrm{kleb}} = 1.10$. This procedure also ensures that the RANS freestream inflow properties are not altered outside the boundary layer. In our prior work, we assumed negligible pressure fluctuations to determine the fluctuations in density, given the fluctuations in temperature. We relax this assumption in this work to allow a user-specified pressure-fluctuation level. We also require that the recycled temperature fluctuations be no greater (in magnitude) than allowed by Morkovin's hypothesis of negligible total-temperature fluctuations (described in detail in [31]). From Morkovin's hypothesis,

$$
\begin{aligned}
C_p T'_{\mathrm{Mork}} = -\Big[&F_{\mathrm{Kleb}}(u_{\mathrm{RANS}} u'_{\mathrm{recyc}} + v_{\mathrm{RANS}} v'_{\mathrm{recyc}} + w_{\mathrm{RANS}} w'_{\mathrm{recyc}}) \\
&+ \tfrac{1}{2} F^2_{\mathrm{Kleb}} \left(u'^2_{\mathrm{recyc}} + v'^2_{\mathrm{recyc}} + w'^2_{\mathrm{recyc}} \right) \Big]
\end{aligned}
\tag{14}
$$

and the recycled temperature fluctuation is limited as follows:

$$
\begin{aligned}
T'_{\mathrm{recyc}}|_{\mathrm{lim}} &= F_{\mathrm{Kleb}} T'_{\mathrm{recyc}} \min\left(1.0, \left| \frac{T'_{\mathrm{Mork}}}{F_{\mathrm{Kleb}} T'_{\mathrm{recyc}}} \right| \right) \\
&F_{\mathrm{Kleb}} T'_{\mathrm{recyc}} \neq 0
\end{aligned}
\tag{15}
$$

The density fluctuation is determined as follows. First, a provisional value of the pressure fluctuation is determined from the recycled density fluctuation:

$$
p'_{\mathrm{prov}} = R[\rho_{\mathrm{RANS}} T'_{\mathrm{recyc}}|_{\mathrm{lim}} + F_{\mathrm{Kleb}} \rho'_{\mathrm{recyc}} (T_{\mathrm{RANS}} + T'_{\mathrm{recyc}}|_{\mathrm{lim}})] \tag{16}
$$

The pressure fluctuation is then limited to be a specified multiple of the pressure (2% in this case):

$$
p'_{\mathrm{prov}}|_{\mathrm{lim}} = (p'_{\mathrm{prov}}) \min(|p'_{\mathrm{prov}}|, 0.02 p_{\mathrm{RANS}}) \tag{17}
$$

and a corrected value of the density fluctuation is determined from the limited pressure fluctuation:

$$
\rho'_{\mathrm{recyc}} = (p'_{\mathrm{prov}}|_{\mathrm{lim}} - \rho_{\mathrm{RANS}} R T'_{\mathrm{recyc}}|_{\mathrm{lim}})/(T_{\mathrm{RANS}} + T'_{\mathrm{recyc}}|_{\mathrm{lim}}) \tag{18}
$$

IV. Calculation Details

A. Test Geometry and Boundary Conditions

The test geometry is a 28-deg compression ramp placed on the floor of the University of Texas Mach 5 blowdown wind tunnel [5]. Experimental error estimates may be found in [5,6]. Several specific ramp configurations, differing primarily in the width of the ramp, were used. The one modeled in this investigation (ramp 3 in [5]) is 3.5 in. wide. Aerodynamic fences are attached to both sides of the ramp. The precise dimensions of the fences are not given in [5], though it is stated that the leading edge of the fence at the tunnel wall extends 2.75 in. upstream of the ramp leading edge. Figure 2 shows isosurfaces of vorticity magnitude (50,000 s^{-1}), shaded by axial velocity. The position of one of the fences is indicated. The effects of the fences are included in the three-dimensional calculations by imposing solid-wall boundary conditions over the portions of the Z_{min} and Z_{max} grid planes that are within the fence area. Otherwise, periodic boundary conditions are imposed at these planes. The mesh spacing in the spanwise Z direction is uniform, thus boundary-layer growth on the fences is not resolved. The tunnel/ramp surface Y_{min} is treated as an adiabatic wall. An extrapolation condition is used at the upper boundary Y_{max} and at the outflow boundary X_{max}. The preceding recycling /rescaling technique is used to provide a time-dependent inflow boundary condition at X_{min}. The computational domain extends from $X_{\mathrm{min}} = 0$ m to $X_{\mathrm{max}} = 0.304$ m in the streamwise direction, from $Z_{\mathrm{min}} = -0.0444$ m to $Z_{\mathrm{max}} = 0.0444$ in the spanwise direction, and from $Y_{\mathrm{min}} = 0$ m to $Y_{\mathrm{max}} = 0.0635$ m (relative to the plate surface) in the vertical direction. The ramp leading edge is located at $X = 0.1905$ m. The baseline mesh contains 360 cells in the X direction, 144 cells in the Y direction, and 129 cells in the Z direction (6.687 million cells in total). The mesh is clustered to the plate surface using a hyperbolic tangent stretching function so that the minimum d_w^+ in the inflow boundary layer is around one. The mesh spacing is uniform in the X and Z directions and is chosen such that approximately 20 cells would be located within one boundary-layer thickness (0.0175 m). One simulation was performed on a mesh with smaller spacing (60% of the baseline value) in the interaction region. This mesh contains 480 cells in the X direction, thus raising the total number of cells to 8.916 million. For the remainder of this paper, the X coordinate is redefined to represent the distance along the surface of the geometry, and the origin is located at the wedge apex. The Y coordinate is redefined to represent the coordinate normal to the surface.

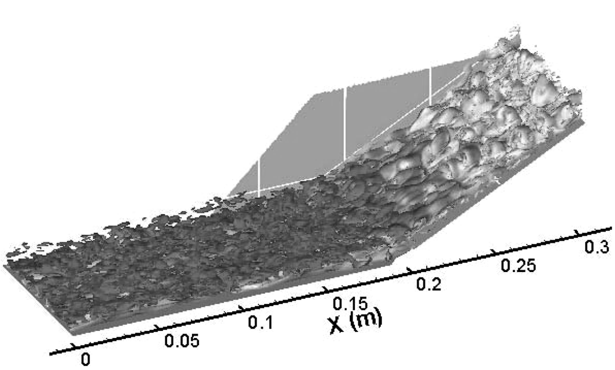

Fig. 2 Isosurfaces of vorticity magnitude shaded by axial velocity.

B. Initialization Procedure and Time-Evolution Details

The calculations were initialized by first computing a 2-D flat-plate solution for the incoming boundary layer. A target inflow profile was determined as the location in which the computed boundary-layer properties best matched the experimental values shown in Table 1.

The test section in the experiments is just downstream of the wind-tunnel nozzle exit. Details of the nozzle geometry were not available, and so the preceding procedure was used to provide a representative inflow. The inflow profile was extracted from the flat-plate data and used to initialize a 2-D RANS calculation of the entire interaction. As discussed in Sec. V.E, the choice of the constant A_{sst} has a pronounced effect on the prediction of the upstream extent of axial separation; the 2-D RANS data corresponding to $A_{\mathrm{sst}} = 0.9$ was used to initialize the three-dimensional hybrid LES/RANS calculations.

Table 1 Inflow boundary-layer properties

Parameter	Value
M_∞	4.95
p_o, Pa	2.17e6
T_o, K	350
Re/m	50.1e6
δ_o, cm	1.75
δ^*, cm	0.63
θ, cm	0.00513
C_f	7.83e-4

To accelerate the development of coherent structures, a velocity-fluctuation field obtained from a previous LES/RANS simulation of a Mach 3 boundary layer at a Reynolds number/meter of 49.5e6 [32] was superimposed upon the RANS base state upstream of the wedge apex. The Mach 3 velocity-fluctuation field was expanded in the periodic Z (spanwise) and assumed periodic X (streamwise) directions to cover the X–Z extent of the flat-plate region. The velocity fluctuations from the Mach 3 simulation were scaled by the ratio of the friction velocities,

$$u_i'|_{M=5} = u_i'|_{M=3}\left(\frac{u_\tau|_{M=5}}{u_\tau|_{M=3}}\right) \tag{19}$$

and all coordinates were scaled by the ratio of the boundary-layer thicknesses,

$$x_i|_{M=5} = x_i|_{M=3}\left(\frac{\delta_0|_{M=5}}{\delta_0|_{M=3}}\right) \tag{20}$$

to provide a reasonable match with the Mach 5 flow. Equation (14) was then used to provide the temperature-fluctuation field, and an assumption of negligible pressure fluctuations was used to provide the density-fluctuation field. Wu et al. [33] reported the use of a similar initialization technique in their DNS calculations.

Starting from this initial condition, a hybrid LES/RANS solution with $A_{\mathrm{sst}} = 0.9$ was evolved at a time step of 2e-7 s for 3.5 ms ($155\delta_0/u_\infty$) to eliminate initial transients. Complete time histories for several planes of data ($Z/\delta_0 = 0.0$, $Y/\delta_0 = 0.0$, $Y/\delta_0 = 0.2$, $Y/\delta_0 = 0.7$, $X/\delta_0 = -3.5$, $X/\delta_0 = 0.0$, and $X/\delta_0 = 4.0$) were then collected for an additional 8 ms ($354\delta_0/u_\infty$). The sampling period was 2e-6 s. Flow-property data were also averaged in time and in space over the interval $-1.8 < Z/\delta_0 < 1.8$ to yield nominally two-dimensional statistics. The solution obtained after 11.5 ms was used as the initial condition for three additional runs: $A_{\mathrm{sst}} = 0.0$, $A_{\mathrm{sst}} = 0.9$ on the refined mesh, and $A_{\mathrm{sst}} = 1.0$. In these cases, the solutions were evolved for 3.0 ms without gathering statistics. Statistics were then collected for a minimum of 8 ms beyond this point.

V. Results and Discussion

A. Flat-Plate Boundary Layer

Axial velocity profiles in wall coordinates are compared with experimental data [5] in Fig. 3. These profiles, as well as those shown in Fig. 4, were extracted at the recycle-plane location ($\sim 7\delta_0$ downstream of the inflow plane). The RANS and hybrid LES/RANS solutions slightly overpredict the experimental data but are virtually indistinguishable from one another. The time-averaged position of the blending function is also indicated. The $\Gamma = 0.9$ position is at $d_w^+ = 266.1$, and the $\Gamma = 0.5$ position is at $d_w^+ = 344.5$. The target d_w^+ location, defined according to the criteria outlined in Sec. III.B, is 345.5, and so it is clear that the predicted average position of the blending function is obtained in the simulations.

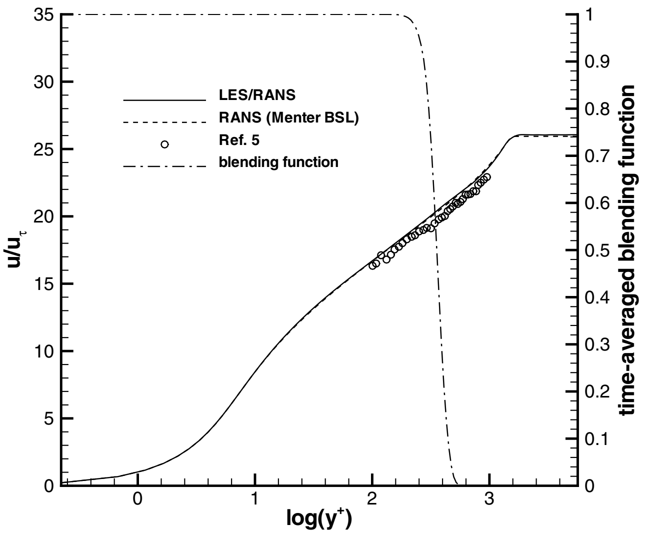

Fig. 3 Inflow boundary-layer velocity profile and blending-function position (wall coordinates).

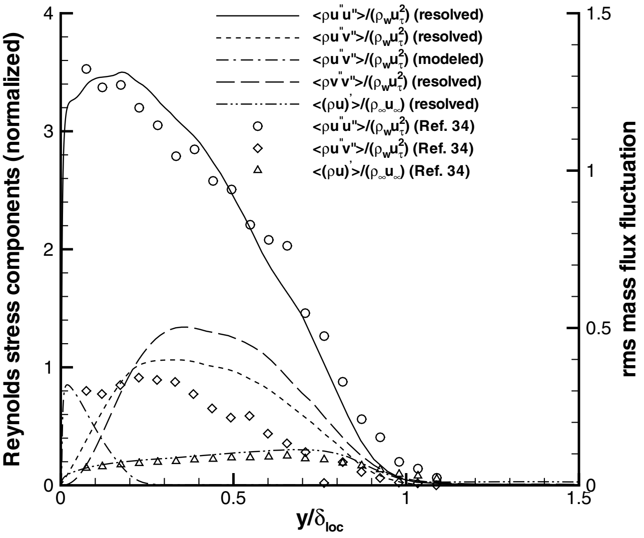

Fig. 4 Reynolds stress and mass-flux-fluctuation profiles in inflow boundary layer

Figure 4 compares Reynolds stress components and rms mass-flux-fluctuation data with experimental data from Smits and Muck [34] at Mach 2.79, $Re/\mathrm{m} = 63.0\mathrm{e}6$, because comparable Reynolds stress data for the actual Mach 5 experiments could not be located. The Reynolds stress components are scaled by $\rho_w u_\tau^2$, whereas the rms mass-flux fluctuation is scaled by $\rho_\infty u_\infty$, thus providing a measure of the turbulence intensity. Agreement with experimental data for the normal stress component $\langle \rho u'' u'' \rangle$ is good, but the predictions for the resolved shear stress component $\langle \rho u'' v'' \rangle$ show a larger constant-stress region (extending to approximately $Y/\delta_{\mathrm{loc}} = 0.4$) than is indicated in the experimental data. This leads to an overprediction of the Reynolds shear stress in the outer part of the boundary layer. The sum of the RANS $\langle \rho u'' v'' \rangle$ component (also shown) and the resolved $\langle \rho u'' v'' \rangle$ component extends the constant-stress region further toward the wall, and the maximum normalized shear stress is around one, as expected from inner-layer scaling theory. The prediction for the normal stress component $\langle \rho u'' v'' \rangle$ also displays a maximum value at $Y/\delta_{\mathrm{loc}} \sim 0.4$, which is outside the logarithmic layer. This unexpected behavior is the subject of current study. The mass-flux-fluctuation profile agrees reasonably well with the experimental data, though the peak value is slightly overpredicted. Except for the Reynolds shear stress response in the outer layer (which could lead to faster boundary-layer growth that anticipated), the equilibrium boundary-layer structure appears to be well-predicted by the hybrid LES/RANS model.

B. Three-Dimensional Flow Structure

Some aspects of the instantaneous flow structure are illustrated in Figs. 2 and 5. Smaller-scale structures seem to be attenuated as the

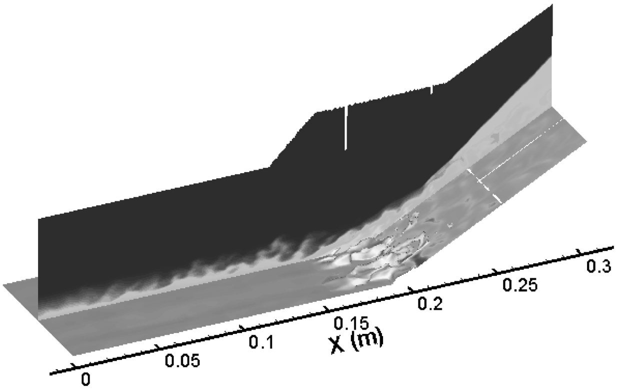

Fig. 5 Isosurfaces of zero axial velocity shaded by temperature.

flat-plate boundary layer shifts to a wakelike pattern upon detaching from the surface, and longitudinal roller-type structures are formed as the shear layer reattaches (Fig. 2). Figure 5 shows an isosurface of zero axial velocity shaded by the mean temperature. The regions of separated flow are not continuous across the span of the domain and they taper to a point when reattaching on the ramp surface. High wall temperatures are found in the vicinity of the reattachment locations.

Time-averaged predictions of wall skin friction are shown in Fig. 6, and corresponding line plots are shown in Fig. 7. Results from three different simulations, $A_{\mathrm{sst}} = 0.0$, $A_{\mathrm{sst}} = 0.9$, and $A_{\mathrm{sst}} = 1.0$, are illustrated in Fig. 6. The incoming boundary layer and the region of reversed flow (darker gray) are nominally two-dimensional. Some small peaks and valleys in the skin-friction distributions are evident upstream of the wedge apex, but the positions are different among the simulations. This indicates that with sufficient time evolution, a statistically two-dimensional flow would probably be obtained upstream of the wedge apex. The situation is different in the reattachment/recovery region. Here, the peaks and valleys in the distributions are much more prominent, with the regions of lower skin friction corresponding to the extension of pockets of low-momentum fluid further onto the ramp surface. In their LES simulation of Mach 3 flow over a compression corner, Loginov et al. [16] also observed this topology and attributed it to the presence of pairs of counter-rotating streamwise vortices in the reattaching shear layer. Experimental oil-flow images presented in [35] also show evidence of these structures. The regions of lower skin friction (lighter streaks) correspond to the action of the vortices in lifting fluid away from the wall, whereas the regions of higher skin friction (darker streaks) correspond to the vortices forcing higher-momentum fluid toward the wall. In the present simulations, the spanwise positioning of the structures correlates with weaker spanwise inhomogeneities in the incoming boundary layer; the same effect is seen in the simulations of Loginov et al. [16]. The distance between lines of convergence (lighter contours) provides a measure of the size of the dominant vortex pairs We find that these sizes range from $\sim 1.2\delta_0$ to $2.0\delta_0$, which may be compared with a value of $\sim 2.0\delta_0$ in the calculations of Loginov et al. Loginov et al. also argued that the growth of these structures may result from a Görtler instability mechanism, given the degree of streamline curvature present as the boundary layer separates, then reattaches on the wedge surface. Navarro-Martinez and Tutty [36] observed the formation and evolution of Görtler-type vortices in simulations of hypersonic laminar flow over a compression ramp. The size of the vortex pairs in their work is approximately the same as the incoming boundary-layer thickness. Because the vortical structures appear to originate from amplification of inhomogeneities present in the inflow boundary layer, the time-averaged positions of the vortices on the ramp surface are likely to depend on the methods used to initiate and sustain the boundary layer and possibly on the total time elapsed during the simulation.

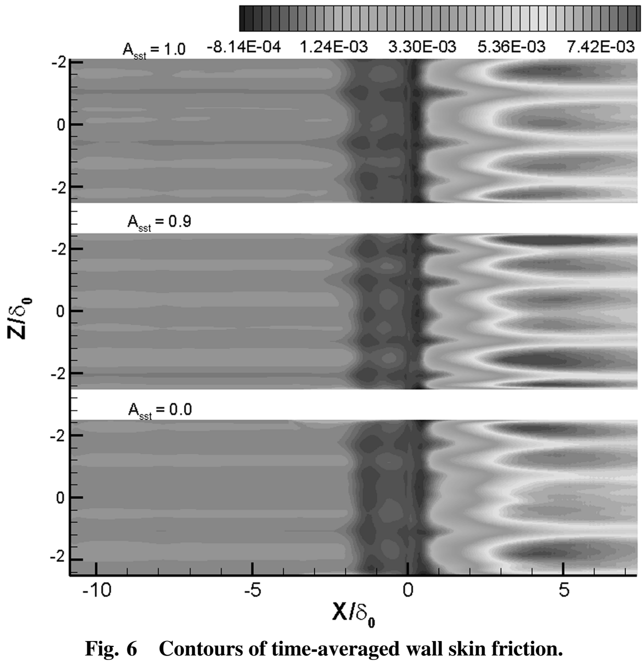

Fig. 6 Contours of time-averaged wall skin friction.

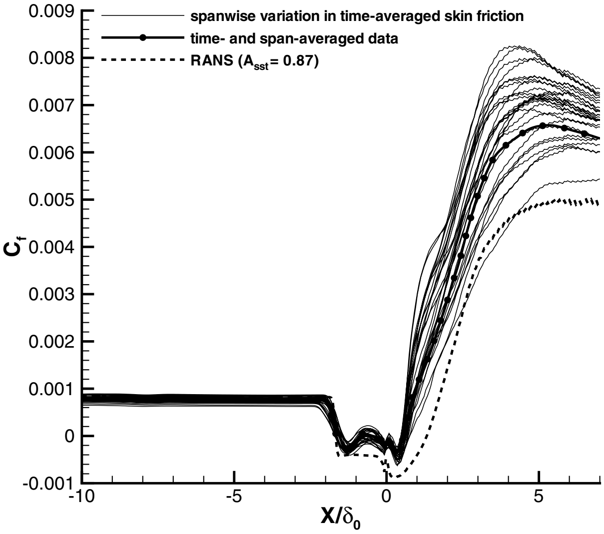

Fig. 7 Spanwise variation of time-averaged skin friction.

Figure 7 presents line plots of time-averaged skin friction at different spanwise positions for the $A_{\mathrm{sst}} = 0.0$ LES/RANS case. Also shown are the span-averaged value and the result from a RANS calculation with $A_{\mathrm{sst}} = 0.87$. As shown later, this choice for A_{sst} provides the best match with the upstream position of the separation shock, as predicted by the LES/RANS method. The degree of spanwise variation about the mean value is noteworthy (-18 to $+26\%$ at the peak location), and at all stations, the skin-friction values in the recovery region exceed those predicted by the RANS model. The high-frequency noise in the skin-friction distributions on the wedge surface is an artifact of a numerical precision problem in the data-reduction code and is not a feature of the computed flowfield. Other comparisons with the RANS models are described in Sec. V.E.

The presence of a range of frequencies in the unsteady motion of shock wave as it interacts with a boundary layer is well-documented in experiments ([1] and references cited within). Turbulent eddies directly interact with the shock wave, producing ripples in the shock front that change their amplitude and positions over time scales representative of the motion of the individual eddies. Less well understood is the presence of a large-scale, low-frequency oscillation of the entire shock system and the associated region of separated flow [1]. Recent wide-field planar light-scattering (PLS) measurements [9,10] and time-resolved particle imaging velocimetry (PIV) measurements [11] suggest that this behavior may be associated with the sustained presence of elongated streaks of uniform-momentum fluid in the incoming boundary layers. These streaks have been shown to extend upward of $30\delta_0$ in a Mach 2 flow [9] and to at least $40\delta_0$ in a Mach 5 flow [10]. In regions in which the streaks have lower momentum than the average, the separation shock can move further upstream; the converse is true in regions in which the streaks have higher momentum than the average. It is argued that the persistence of these streaks allows a low-frequency motion to develop, whereas individual-eddy interactions continue to provide a high-frequency component.

Figure 8 presents snapshots of the axial velocity within a plane located at $Y/\delta_0 = 0.2$. This location corresponds to that chosen for wide-field PLS and PIV imaging in [9–11]. The snapshots are numbered 1–10, with each successive snapshot separated by 0.0001 s. Contour levels are chosen to highlight regions of lower velocity (dark) and higher velocity (light) in the incoming boundary

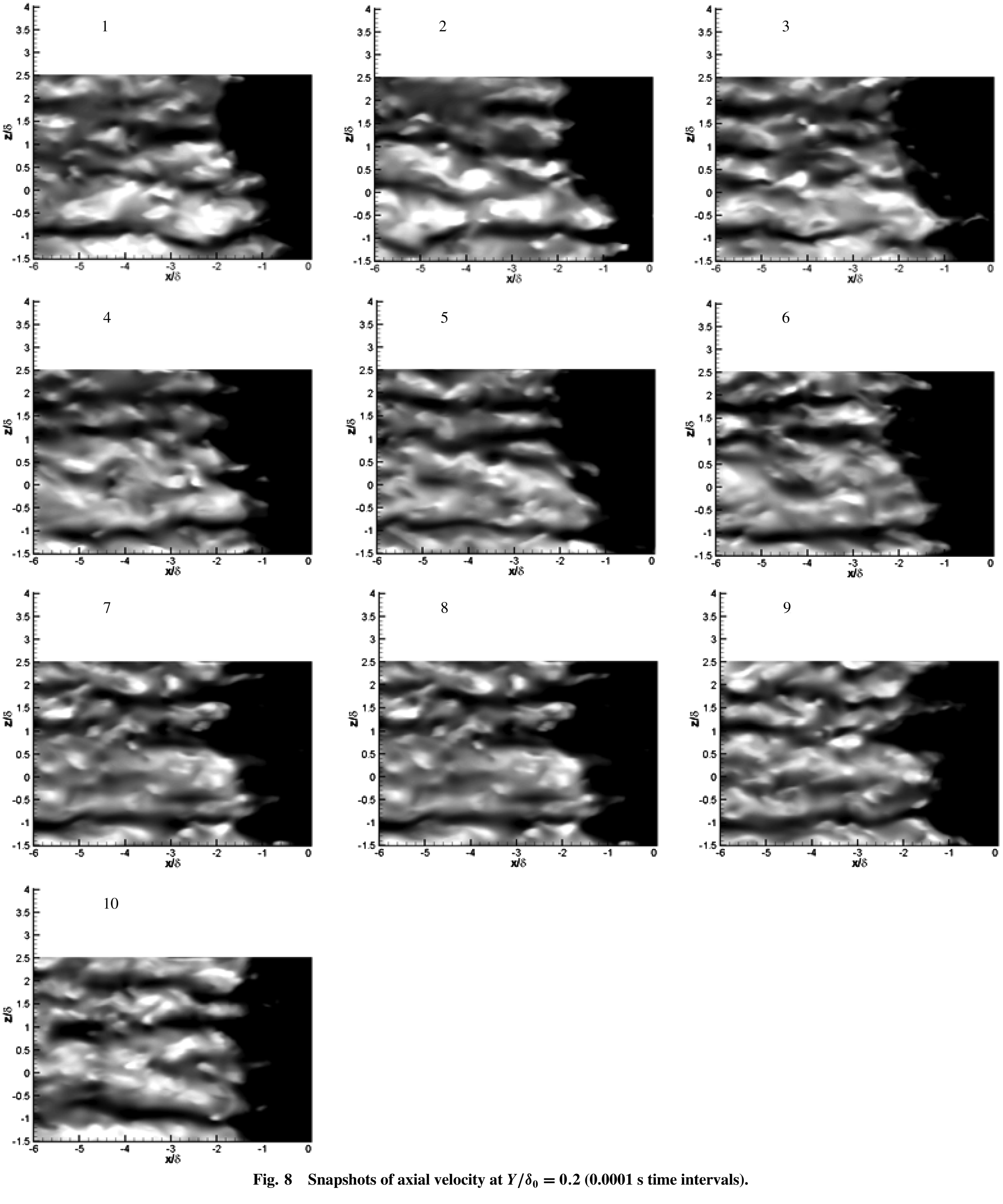

Fig. 8 Snapshots of axial velocity at $Y/\delta_0 = 0.2$ (0.0001 s time intervals).

layer. The separation region is identified as the start of the dark black region at the left of the figures. There is clear evidence of a streaklike pattern in the incoming boundary layer. Frames 1–6 in the snapshot sequence (extracted from the $A_{\mathrm{sst}} = 0.9$ simulation on the baseline mesh) show that the separation region is located further upstream toward the upper side fence (top) and that this upstream positioning is correlated with a general darkening of the contours, indicating the sustained presence of lower-momentum fluid. At later times (frames 7–10), higher-momentum streaks of fluid eventually enter this region and act to push the separation line further downstream. The separation region near the lower side plane does not migrate as much over this time interval. The passage of individual streaks of fluid into the separation zone results in local perturbations to the separation line, but it is the collective effect of several neighboring streaks with approximately uniform momentum that appears to induce the larger-scale dynamics. This conclusion was also reached in [11].

Figure 9 presents snapshots of the velocity field averaged over successive periods of 0.001 s. Frame 2 in this sequence corresponds to the event illustrated in detail in Fig. 8. Frames 1, 3, and 4 indicate the effects of isolated streaks of low/high momentum fluid in locally modulating the separation region, and the collective effect of a group of higher-momentum streaks in pushing the separation region further downstream is shown at the bottom of frame 5.

Figure 10 presents snapshots of vertical v velocity contours in the interaction region, extracted every 0.001 s along the $Z/\delta_0 = 0.0$ center plane from the $A_{\mathrm{sst}} = 0.0$ simulation data. The view corresponds approximately to that imaged at the University of Texas [8] using time-resolved PLS techniques. The snapshots show a highly dynamic motion of the separation shock. Its progression forward (frames 4, 6, and 8) appears to be accompanied by the thickening of the separation region (indicated in dark contours), whereas its travel upstream (frames 1 and 3) is associated with the elongation and thinning of the separation region. The boundary layer changes dramatically as the fluid moves through the separation shock and reattaches on the ramp surface. Animations of the interaction reveal that larger, more two-dimensional, eddies form in the wakelike region above the separation zone, and their passage downstream deforms the reattachment-shock plane significantly.

The preceding discussion provides some evidence that LES/RANS calculations performed at high Reynolds numbers can qualitatively capture some of the near-wall features that may contribute to low-frequency separation-shock unsteadiness. A more quantitative assessment that correlates the time scales associated

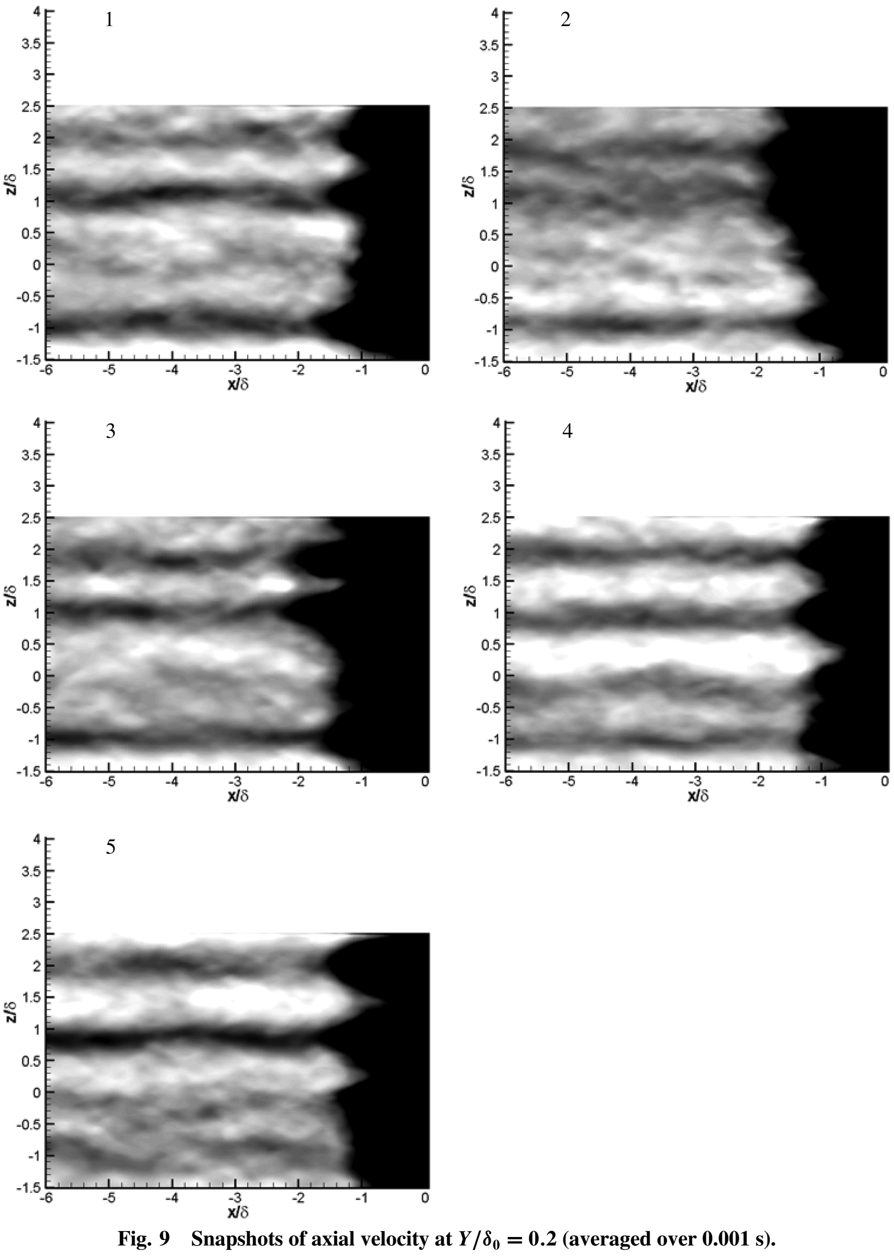

Fig. 9 Snapshots of axial velocity at $Y/\delta_0 = 0.2$ (averaged over 0.001 s).

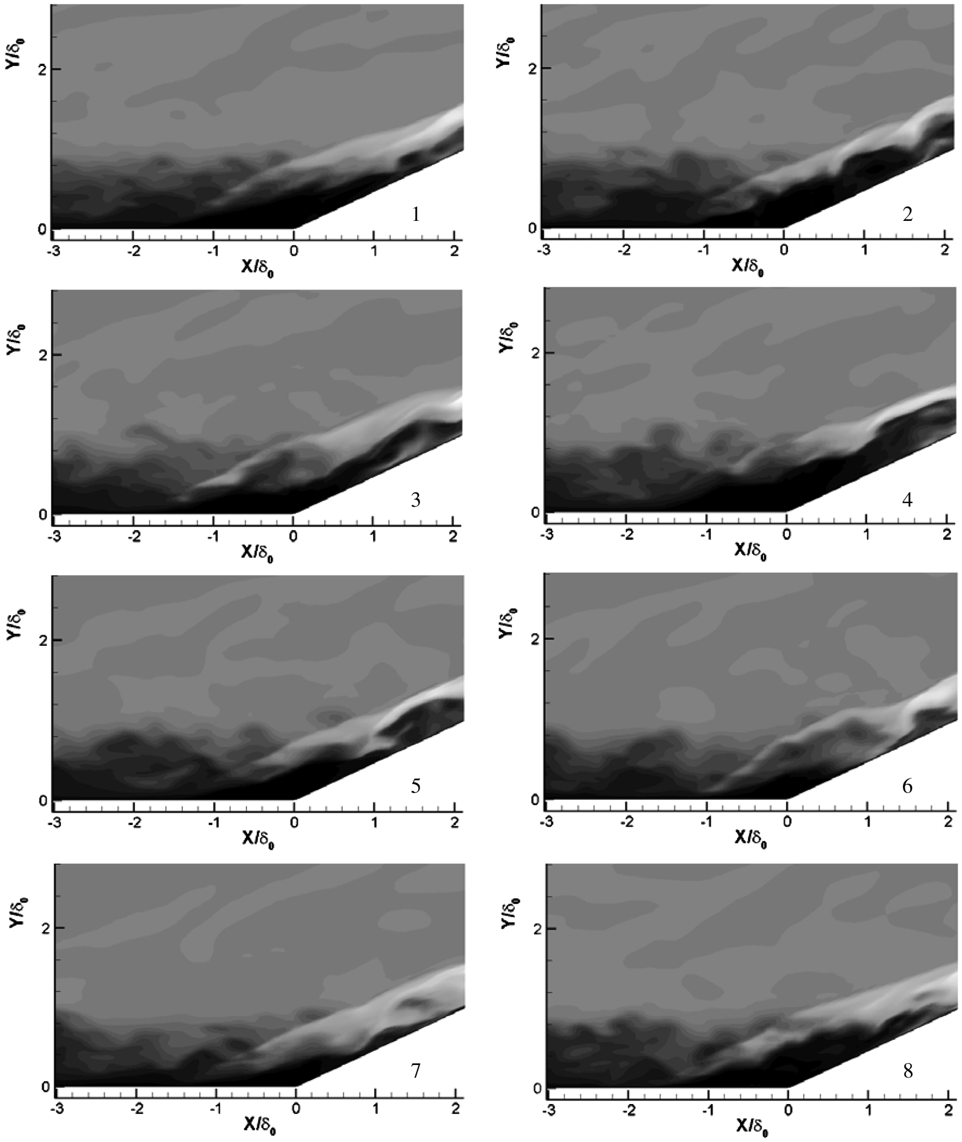

Fig. 10 Snapshots of vertical velocity in *X–Y* center plane (0.001-s time intervals).

with the passage of streaklike structures with the observed low-frequency spectrum is difficult for several reasons. First, to obtain good statistics for the low-frequency spectrum, one would have to run the calculations much further in time (several hundredths of seconds). Second, even if this is done, the use of recycling/rescaling would appear to force a length scale equal to the distance between the inflow plane and the recycling plane $7\delta_0$ onto the computed flow, and it is possible that the streak lengths may be elongated artificially as a result. Our application of Taylor's hypothesis to extract estimates of the lengths of the near-wall structures (not shown, but available upon request) showed that the streaklike structures extending 50 to $100\delta_0$ were present, but this analysis is questionable, based on the reasons mentioned previously. The fact that the $Y/\delta_0 = 0.2$ plane is in the RANS/LES transition region also induces a degree of uncertainty. Other aspects of the interactions, such as the level of upstream influence present and the three-dimensional structure of the separation bubble, may also contribute to the observed low-frequency response [37,38].

C. Comparisons with Experimental Mean-Flow Data

Mean flowfield data obtained in the Dolling-group experiments [5,6] include average wall pressure distributions (some conditioned on the separation-shock position), pressure-fluctuation variance distributions, and pitot pressure distributions in the reattachment region. Most of these measurements were taken along the centerline of the configuration. To generate smoother statistics and thereby approximate a longer time sequence than is actually available in the simulations, we elected to average most of data over the interval $-1.8 < Z/\delta_0 < 1.8$ in the spanwise direction. This eliminates regions of the flow that are nearest to the fences from directly affecting the time averages.

Wall pressure distributions are shown in Fig. 11 for each of the LES/RANS simulations. Several trends are apparent. Although the general shape of the pressure distribution upstream of the wedge is predicted accurately, all of the calculations underpredict the pressure level in this region. Because the separation-shock pressure rise, in a time-averaged sense, is related to the displacement effect of the separation bubble, this trend indicates that no approach correctly predicts the vertical extent of the separation region. The separation-shock pressure rise appears to take place gradually over a distance of about 1 to $1.5\delta_0$. This response is a result of the averaging effects of the separation-shock motion, and all predictions capture this feature to good accord. The $A_{\mathrm{sst}} = 0.0$ calculation provides the best overall agreement with the experimental data in the separation region, even though the upstream extent of the separation bubble is slightly underpredicted. The $A_{\mathrm{sst}} = 1.0$ calculation results in an elongated separation bubble that provides only a small displacement effect. The $A_{\mathrm{sst}} = 0.9$ calculations performed on the baseline and refined meshes provide generally similar results, but it is clear that localized mesh refinement does not improve agreement with experimental data. The pressure level on the wedge surface is in excess of that measured in

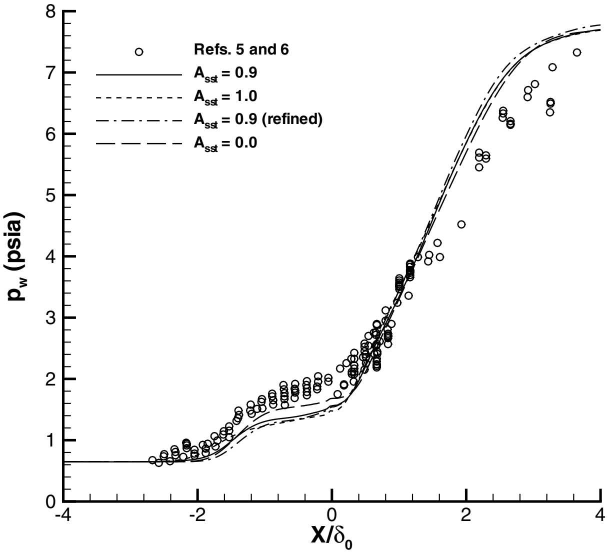

Fig. 11 Wall pressure distributions (LES/RANS models).

the experiments. This is a consequence of the underprediction of the size of the separation region and the separation-shock strength.

Other differences between the model predictions are noted in Fig. 12, a plot of time-averaged axial velocity contours in the interaction region. The vertical axis is the normal distance from the surface. As such, there is a discontinuity at the wedge apex, and all data are interpolated onto normal lines extending away from the surface. Also shown in the comparison is a prediction from the baseline RANS model with $A_{\mathrm{sst}} = 0.87$. The enhanced vertical displacement of the separation bubble in the $A_{\mathrm{sst}} = 0.0$ LES/RANS calculation, relative to that of the $A_{\mathrm{sst}} = 1.0$ calculation, is clearly indicated. The bubble size and shape in the $A_{\mathrm{sst}} = 0.0$ LES/RANS calculation is comparable with that predicted by the RANS model.

Predictions of the standard deviation of the wall pressure fluctuations are presented in Fig. 13. The general shape of the experimental distribution is captured, but the peak in fluctuation intensity near the separation shock is underpredicted by all models. The $A_{\mathrm{sst}} = 0.9$ calculation on the baseline mesh best predicts the position of the peak. It should be noted that the magnitude of the peak (but not its location) is well-predicted by the $A_{\mathrm{sst}} = 0.0$ calculation if the data are sampled at $Y/\delta_0 = 0.2$ instead of at the wall. This result may imply that the enhanced eddy viscosity provided by RANS model in the near-wall region damps the separation-shock motion to some degree. All calculations capture the fluctuation-intensity level in the pressure-plateau region upstream of the corner, but all overpredict the intensity level in the reattachment and recovery regions. Because the wall pressure itself is also overpredicted in this region, it is useful to examine the rms values normalized by the local wall pressure. Figure 14 shows that none of the calculations correctly capture the relative distributions of fluctuation intensity due to separation-shock motion and due to shear layer reattachment and reattachment-shock motion. Whereas the underprediction of the peak in fluctuation intensity near the separation shock may be due to the damping effect of the near-wall RANS model, the opposite may be true on the ramp surface.

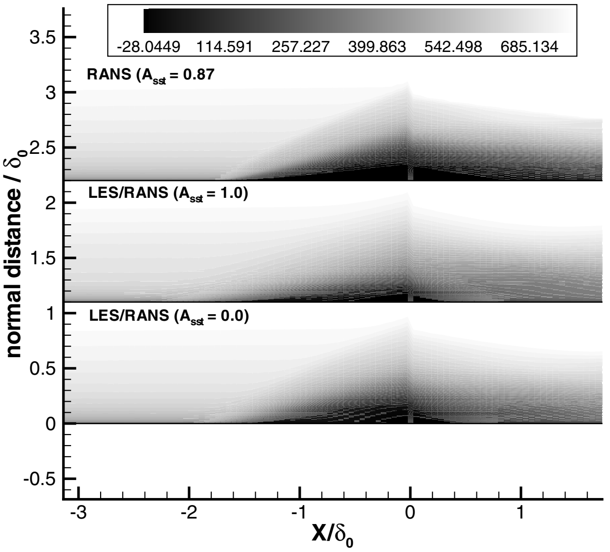

Fig. 12 Time-and span-averaged axial velocity contours in the interaction region.

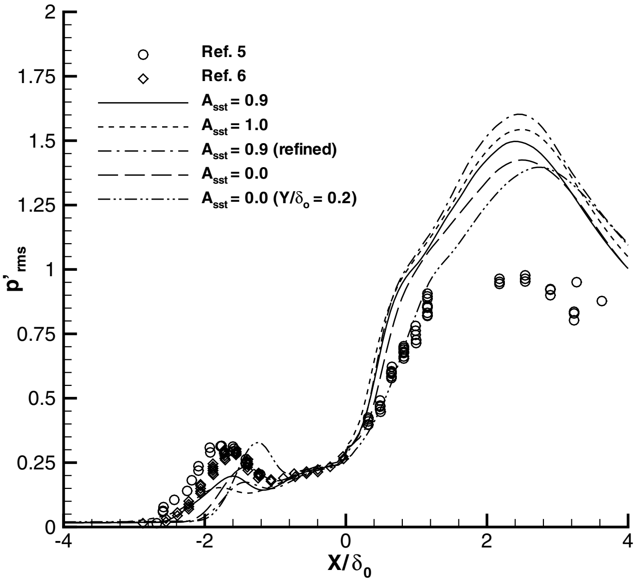

Fig. 13 The rms pressure-fluctuation distributions (hybrid LES/RANS models).

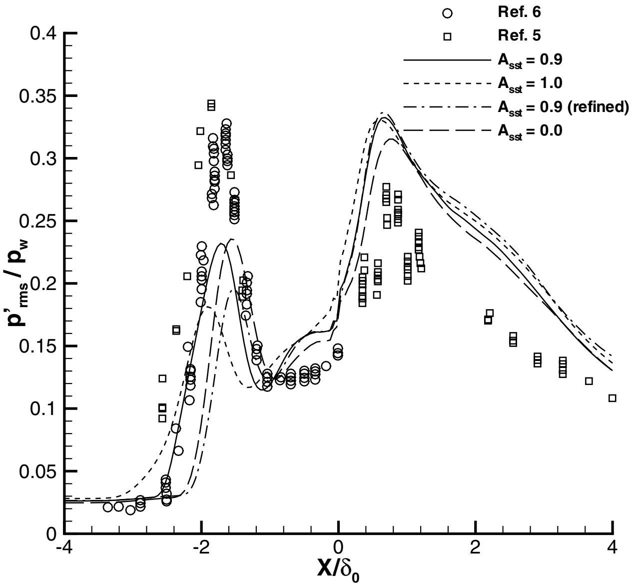

Fig. 14 The rms pressure-fluctuation distributions normalized by local wall pressure.

Figure 15 plots the time- and span-averaged blending function in the interaction region. Also shown in the figure is the blending function as determined using the RANS basic state (see Sec. III.B). Downstream of reattachment, the blending function collapses toward the wall, meaning that more of the recovering boundary layer is modeled as a large-eddy simulation. The near-wall resolution may be

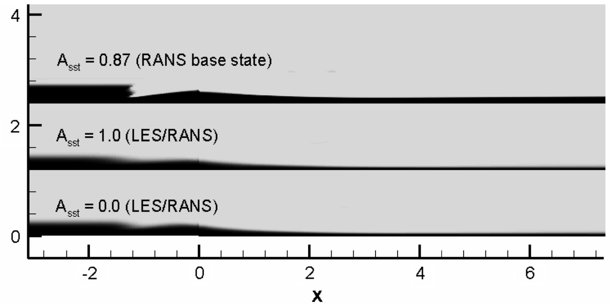

Fig. 15 **Time- and span-averaged blending functions in the interaction region (vertical coordinate is normal to the surface).**

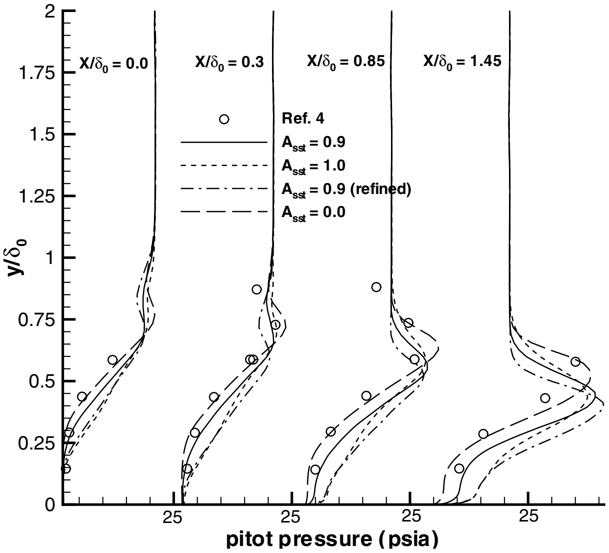

Fig. 16 **Pitot pressure profiles in reattachment region.**

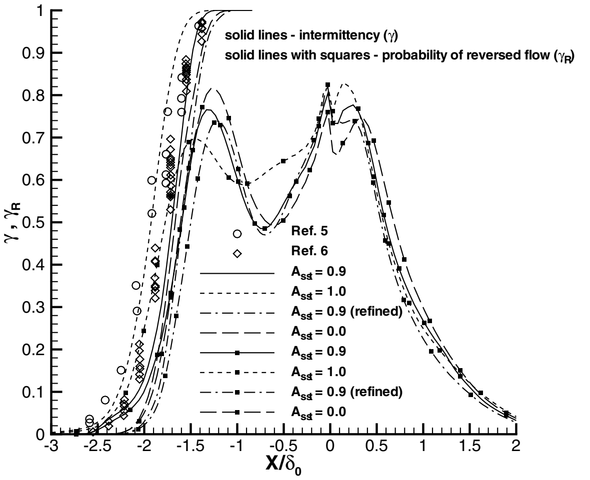

Fig. 17 **Separation-shock intermittency and probability of reversed flow.**

insufficient to capture the proper decay of turbulence energy, and the fluctuation-intensity level at the surface may be overpredicted as a result. The collapse in the blending function is a direct result of an increase in the turbulence frequency ω as the flow passes through the shock system. The blending function as determined using the RANS basic state responds in a similar way, but the transition is sharper and the transition location is generally further away from the surface. Even with this effect, it is likely that further improvements in the prediction of the separation-shock strength and the upstream extent of the separation zone would result in better predictions of the fluctuation intensity throughout the interaction.

Predictions of pitot pressure at several stations just downstream of the corner are compared with experimental data from [4] in Fig. 16. The best result is provided by the $A_{\mathrm{sst}} = 0.0$ calculation, which captures the wakelike structure of the reattaching boundary layer correctly at all positions. For the other models, the peaks in the pitot pressure distribution are positioned closer to the wall and the boundary layer appears to accelerate more rapidly than is indicated in the experimental data.

D. Dynamics of Shock-System Motion

References [5,6] describe the use of conditional sampling techniques to examine the motion of the shock-induced separation region and the resulting effects on the wall pressure profiles. We performed similar analyses using the wall pressure data extracted in the LES/RANS simulations. Again, spatial homogeneity was assumed over the $-1.8 < Z/\delta_0 < 1.8$ interval to increase the sample size. Figure 17 shows the intermittency of the separation-shock position. At a particular X station, the intermittency γ is defined as the fraction of time that the separation shock is ahead of this position. A value slightly greater than zero corresponds to the most upstream positioning of the separation shock, whereas a value slightly less than one corresponds to the most downstream positioning of the separation shock. The most probable position of the separation shock is indicated by an intermittency value of 0.5. The separation shock is identified by first computing a normalized pressure

$$\bar{p}(x) = \frac{|p(x) - p_\infty|}{p_\infty}$$

This is then limited so that $\bar{p}(x)$ is set to zero if $\bar{p}(x) < 0.25$. We then search along a line in the X direction until we find the coordinate for which $\bar{p}(x)$ changes from zero to a positive value. This location is identified as the separation-shock position. The general shape of the experimental intermittency distribution is captured by all LES/RANS models, though the extent of the separation-shock motion appears to be slightly underpredicted. The most probable position of the separation shock in the experiment is around $-1.8X/\delta_0$; the $A_{\mathrm{sst}} = 1.0$ prediction ($-1.95X/\delta_0$) and the $A_{\mathrm{sst}} = 0.9$ prediction on the baseline mesh ($-1.7X/\delta_0$) bracket the experimental result.

Figure 17 also shows γ_R as a measure of the probability of having reversed axial flow near the surface. This quantity is calculated from data extracted at the first X–Z plane away from the surface. A value of 1 at a given location means that for the entire sample time, the axial velocity is negative. As shown, there is no station that maintains reversed flow at all times, and at all stations within the separation zone, there is at least a 20% probability of having positive axial flow near the surface. In the region of separation-shock intermittency, the probability of reversed flow ranges from near zero at $\gamma = 0$ to 0.8 at $\gamma = 1$. From this, it can be concluded that the most downstream positioning of the separation shock is strong enough to immediately separate the boundary layer, whereas the separation shock at its most upstream location is weaker and does not immediately induce reversed flow. Further downstream, the probability of reversed flow decreases to a value of about 0.5 before increasing again to a value of 0.8 near the wedge apex. A nonzero probability of having reversed flow exists on the wedge surface past $X/\delta_0 = 2.0$. This is associated with the effect of the counter-rotating vortices discussed in Sec. V.B in moving fluid away from the surface.

Conditional pressure distributions may be obtained by “binning“ streamwise wall pressure traces according to the position of the separation shock. Figure 18 compares pressure distributions corresponding to $\gamma = 0$ to 0.05 (the most upstream positioning of the shock) and $\gamma = 0.95$ to 1.0 (the most downstream positioning) versus experimental data. Good agreement is generally achieved for the most downstream positioning of the separation shock, with the $A_{\mathrm{sst}} = 0.0$ calculation providing the best prediction. The $A_{\mathrm{sst}} = 1.0$ calculation correctly predicts the separation-shock position for the $\gamma = 0$ to 0.05 range, but the pressure level just upstream of the wedge apex is underpredicted and the pressure level on the ramp surface is overpredicted. These trends again relate to deficiencies in predicting the displacement effects of the separation bubble.

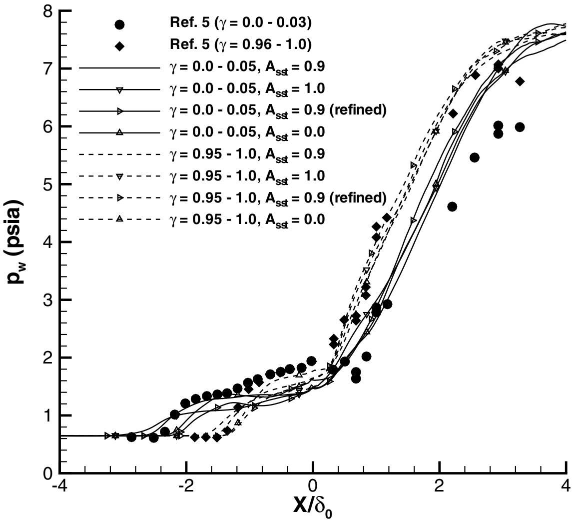

Fig. 18 Conditionally-averaged surface pressure distributions.

Figure 19 presents power spectra obtained at several X stations from pressure data extracted at $Y/\delta_0 = 0.2$. The $A_{\text{sst}} = 0.9$ database on the baseline grid is used in these calculations; similar results are obtained for the other databases. As before, the ensemble of data in the interval $-1.8 < Z/\delta_0 < 1.8$ is used. Each power spectrum is normalized by the variance of the pressure signal and the frequency, as in [5]. Estimated large-eddy frequencies in the incoming boundary layer (based on δ_0 and u_∞) are on the order of 40–50 kHz. The spectrum at $X/\delta_0 = -3.02$ shows that the frequencies containing most of the energy content lie in the range from 15 to 50 kHz. This is in good agreement with results reported in [5] (Fig. 40). For X stations in the intermittent region, the dominant frequencies are much lower: ~0.3 to 1 kHz. This is also in good agreement with the results of Gramann [5] (Fig. 55), which show a dominant band of low-frequency tones ranging from ~0.2 to 2 kHz. Downstream of the wedge apex, the lower-frequency tones diminish, and a higher-frequency spectrum emerges. The dominant frequencies in the ramp boundary layer lie in the interval from ~8 to 30 kHz, which is in good agreement with Gramann's [5] data (Fig. 106). The shift to lower frequencies (relative to those in the incoming boundary layer) may be attributed to the reduced convection speed of eddies downstream of the shock system, because the eddy sizes appear to be similar in the calculations. At all stations, a selection of tones with frequencies ranging from 5 to 7 kHz is seen. These appear to coincide with the recycling frequency, which is approximately equal to $u_\infty/(7\delta_0)$. This band of frequencies is not dominant at any location, though its relative importance does appear to increase in the reattachment/recovery region. Excepting the presence of the recycling frequency, the predictions are in close agreement with experimental observations, indicating that the hybrid LES/RANS model is capable of capturing both low- and high-frequency dynamics of the interaction.

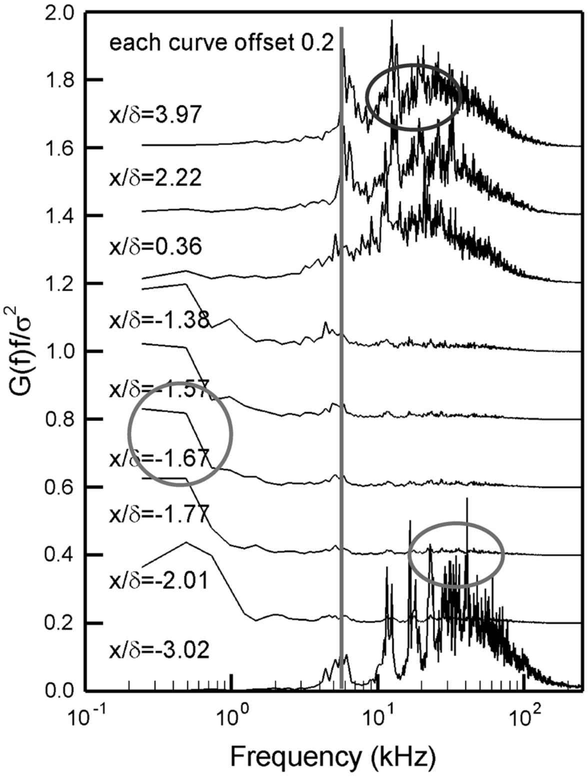

Fig. 19 Power spectra at different streamwise stations.

E. Comparisons with RANS Mean-Flow Data

It is useful to compare predictions obtained by the baseline RANS model with those provided by the LES/RANS model. If the LES/RANS model can be proven more accurate, then it may be possible to use LES/RANS data to evaluate modeled forms for various closure terms appearing in RANS models and from that, it is hoped, to improve their predictive capability. Figure 20 shows the sensitivity of the wall pressure distributions predicted by the RANS model to the choice of the scaling constant A_{sst}. As noted, a value of $A_{\text{sst}} = 0.0$ results in the appearance of a small separation bubble, whereas the choice of $A_{\text{sst}} = 1.0$ results in a very large separation region. This level of sensitivity is much larger than that exhibited by the LES/RANS model (Fig. 9). The best agreement with experimental data is achieved when A_{sst} is set to 0.9, whereas a value of $A_{\text{sst}} = 0.87$ provides a good comparison with the best LES/RANS prediction ($A_{\text{sst}} = 0.0$). Skin-friction distributions in Fig. 21 indicate that the RANS models consistently predict larger (in magnitude) near-wall velocities in the back flow region, compared with the LES model. The RANS solutions also exhibit a delayed reattachment and a slower rate of recovery in the inner layer, compared with the LES/RANS solution. Pitot pressure profiles shown in Fig. 22 indicate that none of the RANS models predicts the experimental trends as closely as the LES/RANS model with $A_{\text{sst}} = 0.0$. The best agreement, not coincidentally, is provided by the $A_{\text{sst}} = 0.87$ RANS solution. Axial velocity profiles at different streamwise stations in Fig. 23 reveal relatively close agreement between the $A_{\text{sst}} = 0.87$ RANS solution and the $A_{\text{sst}} = 0.0$ LES/RANS solution upstream of the wedge apex. However, the transport of momentum toward the surface in the reattachment region ($X/\delta_0 = 2.0$) is clearly larger for the LES/RANS solution. The velocity profile further downstream ($X/\delta_0 = 7.0$) is fuller and flatter as a result, and the reduction in velocity due to wall shear is confined to a very thin layer near the surface. The velocity field does not return to an equilibrium profile within the extent of the domain for either model. In the absence of

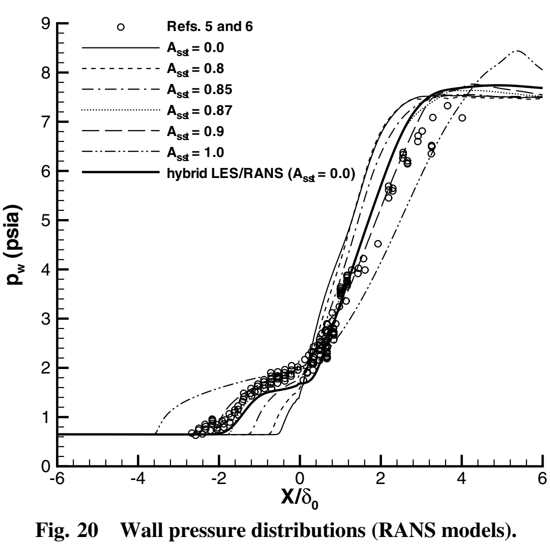

Fig. 20 Wall pressure distributions (RANS models).

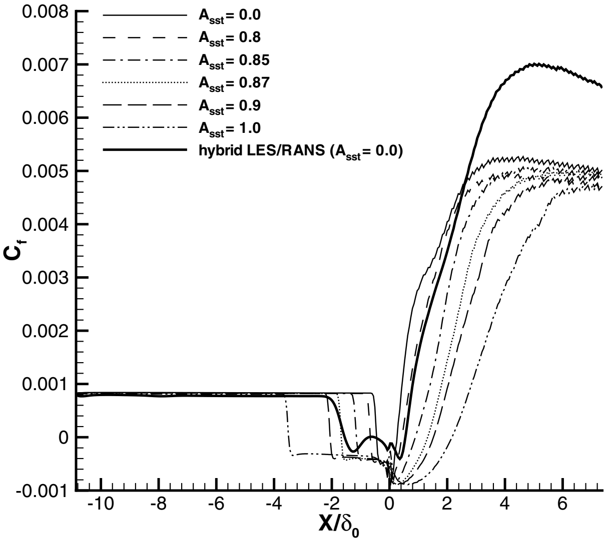

Fig. 21 Skin-friction distributions (RANS models).

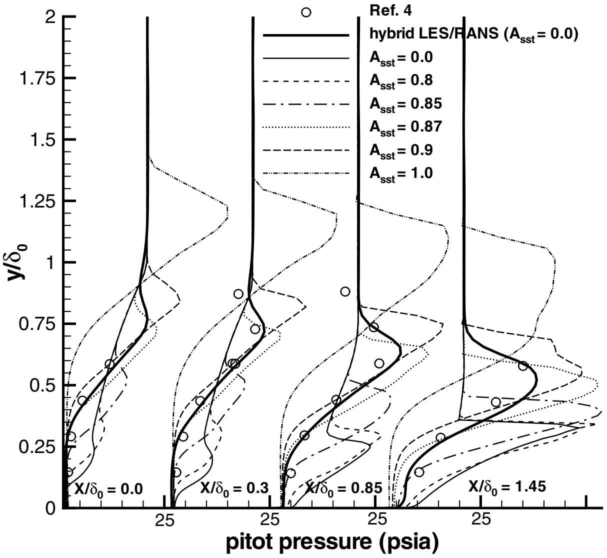

Fig. 22 Skin-friction distributions (RANS models).

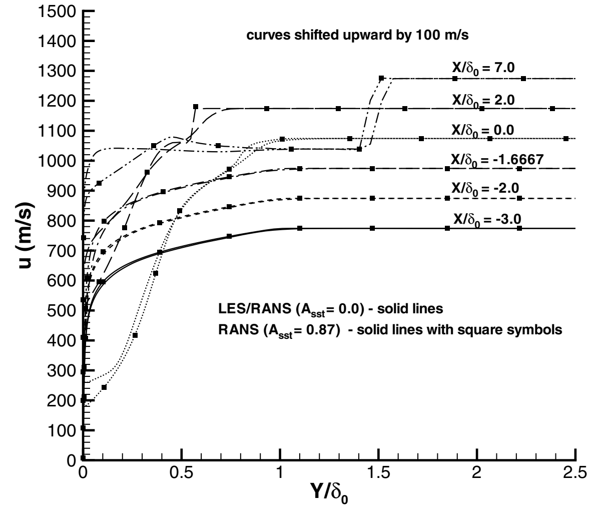

Fig. 23 Axial velocity profiles throughout the interaction.

experimental data downstream of $X/\delta_0 = 2.0$, it is difficult to judge which approach might provide the more correct response, but other experimental studies at Mach 3 [39,40] have measured fuller, flatter boundary-layer profiles in the recovery region. Moreover, earlier hybrid LES/RANS calculations [19–21] have been able to capture the experimental trends, whereas RANS models have not.

F. Comparisons with RANS Reynolds Stress Data

Figure 24 presents the evolution of rms mass-flux-fluctuation $\langle[(\rho u)']^2\rangle^{1/2}$ profiles throughout the interaction region. Fluctuations are amplified by about a factor of 10 near the reattachment position before reducing to a factor of about 7 near the end of the ramp. Maximum mass-flux amplification factors of about 4 are reported for the Mach 3 experiments of Smits and Muck [34] and Zheltovodov et al. [40] and for the computations of Loginov et al. [16].

Contour plots of $\langle\rho k\rangle$, where k is the turbulence kinetic energy per unit mass, are shown in Fig. 25 for the LES/RANS model with $A_{\text{sst}} = 0.0$ and the RANS model with $A_{\text{sst}} = 0.87$. Only the resolved part of $\langle\rho k\rangle$ is presented for the LES/RANS model. The plots shows that amplification of the turbulence kinetic energy begins upstream of the wedge, with the maximum value in this region located within the shear layer that develops above the separation bubble. The turbulence-amplification effect continues as the shear layer reattaches, and the turbulence kinetic energy reaches its maximum value in the vicinity of the reattachment shock. Clearly indicated in the LES/RANS results is the effect of the shock motion in enhancing the amplification rates and in broadening the turbulence kinetic energy distribution. Further downstream, the turbulence kinetic energy begins to decay, and the peak values near the end of the

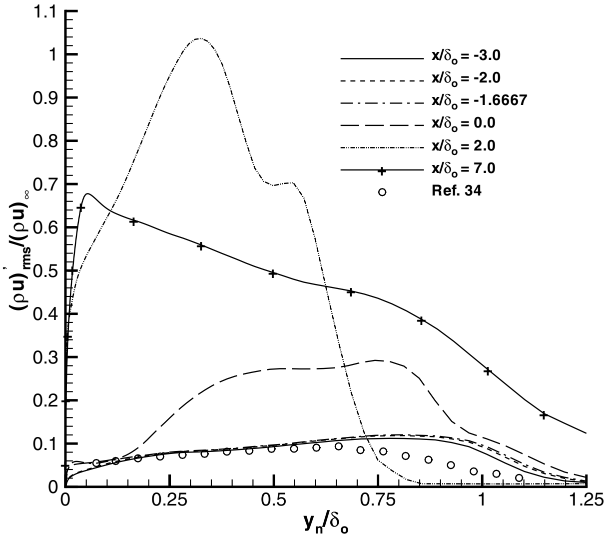

Fig. 24 The rms mass-flux-fluctuation profiles throughout the interaction.

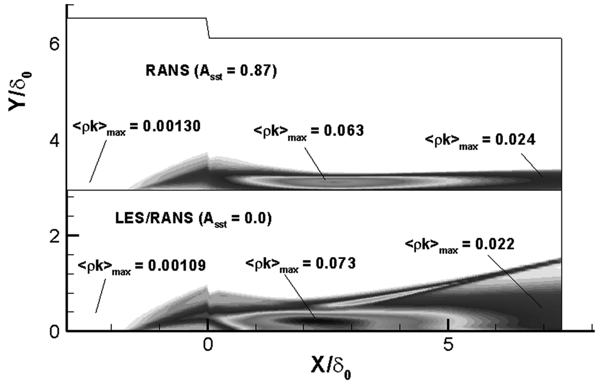

Fig. 25 Contours of turbulence kinetic energy (normalized by $\rho_\infty u_\infty^2$).

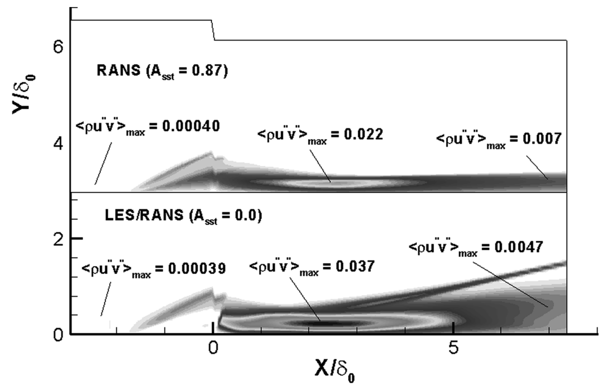

Fig. 26 Contours of Reynolds shear stress (normalized by $\rho_\infty u_\infty^2$).

domain for the LES/RANS and RANS models are comparable. The distribution of turbulence kinetic energy in the normal direction is much wider for the LES/RANS calculation, and the peak is located well away from the surface. This may be due to convection of turbulence kinetic energy into the outer part of the recovering boundary layer, because the mean velocity gradient in this region is relatively small (Fig. 23). The RANS result displays the expected trend of locating the maximum turbulence kinetic energy nearer the wall at which the predicted mean velocity gradient is larger. The maximum amplification factor (relative to the turbulence kinetic energy level in the middle part of incoming boundary layer) is around 67 for the LES/RANS calculation and around 48 for the RANS calculation. The amplification factors reduce to 20 and 18 for the LES/RANS and RANS calculations, respectively, toward the end of the ramp. These values are much larger than the eightfold amplification observed in the Mach 3 experiments of Smits and Muck [34] for the Reynolds normal stress. In the Mach 3 experiments, the compression fan that forms downstream of the reattachment position does not coalesce into a shock within the boundary layer, whereas in the Mach 5 calculations (and probably in the experiment), the coalescence of the compression fan into a shock takes place close to the wall, and the coalesced shock interacts dynamically with the reattaching shear layer.

Contours of the Reynolds shear stress $\langle \rho u' v' \rangle$ are shown in Fig. 26. The Reynolds stress tensor is rotated so that the shear component is tangential to the surface. Upstream of the wedge apex, the LES/RANS model predicts the maximum value of the shear stress as occurring toward the outer edge of the separating shear layer, whereas the separation region is associated with small values of the Reynolds shear stress. The RANS model displays the expected trend of a maximum Reynolds shear stress for which the velocity gradient is largest. Downstream of the wedge apex, the trends generally follow that evidenced for the turbulence kinetic energy. The maximum amplification factors are even larger: 95 for the LES/RANS calculation and 55 for the RANS calculation. These reduce to factors of 12.5 and 17.5 for the LES/RANS and RANS calculations near the end of the ramp. Loginov et al. [16] report a maximum Reynolds shear-stress amplification of 28 in their calculations. The structure factor $\langle \rho u' v' \rangle / \langle \rho k \rangle$, evaluated at the location of maximum Reynolds shear stress toward the end of the ramp, is about 0.265 for both models, indicating that both computed boundary layers may be returning toward equilibrium but through different paths. The locations of the maximum Reynolds shear stress differ significantly, with the LES/RANS calculation placing this location further away from the wall than the RANS calculation. Additional experimental data would be required to determine which modeling approach best captures the evolution of the Reynolds stress tensor for this flow.

VI. Conclusions

Simulations of a Mach 5 compression-corner interaction at $Re/\mathrm{m} = 50.1\mathrm{e}6$ were performed using a hybrid large-eddy/Reynolds-averaged Navier–Stokes (LES/RANS) model. The model uses a flow-dependent blending function to shift the closure from Menter's two-equation RANS model near walls to a Smagorinsky subgrid closure model in the outer part of the boundary layer. The blending function is based on a modeled form of the Taylor microscale and is designed to transition to LES toward the outer part of the logarithmic region (for equilibrium boundary layers). A recycling/rescaling technique, applied to the fluctuating fields, is used to initiate and sustain large-eddy motion. The following conclusions may be stated:

1) The LES/RANS models capture the mean-flow and time-dependent structure of the interaction reasonably well. Observed deficiencies relate primarily to an underprediction of the size of the separation region (particularly its vertical extent), which causes a smaller separation-shock pressure rise and a larger reattachment-shock pressure rise than observed experimentally.

2) The LES/RANS results are sensitive to the amount of SST included in the Menter model: the calculations performed without the SST modification are in better agreement with experimental data. Inclusion of the SST effect improves predictions of the upstream influence of the shock system but reduces the vertical displacement of the separation region. The separation-shock pressure rise is lessened and its dynamics are not as vigorous as a result.

3) In accord with recent LES results at Mach 3 [14], the current work predicts significant three-dimensional effects in the time-averaged flow downstream of the reattachment position. These appear to relate to the formation of counter-rotating vortex pairs in the reattaching boundary layer. The positions of these vortical structures do not migrate substantially over the time intervals considered.

4) Recent conjectures [9–11] relating to the development of a low-frequency motion of the entire shock system due to the persistence of streaks of fluid with lower or higher momentum than the average are supported by the current simulations. In the simulations, it appears to be the collective effect of several neighboring streaks that induces a low-frequency undulation in the separation-shock front. The passage of individual streaks of fluid through the front produces localized ripples but not large-scale motion.

5) The dynamics of the shock-system motion, as quantified by conditional pressure distributions, shock-position intermittency distributions, and power spectra analysis at different locations, were predicted to good accord by the LES/RANS model. The use of a RANS component near the surface does appear to mitigate the near-wall motion of the separation shock to some degree. Upon reattachment, however, the RANS region is forced closer to the wall, and there are indications that the model may not provide enough damping of fluctuations in this region.

6) Calculations performed using the baseline Menter RANS model are much more sensitive to the amount of shear stress transport included. The RANS calculations also predict reattachment as occurring further downstream than seen in the experiment or in the LES/RANS predictions, and the rate of recovery of the boundary layer in the near-wall region is not as rapid as observed in the LES/RANS models or in the experimental results available. Both models predict substantial amplification of Reynolds normal and shear stresses downstream of reattachment, but the distribution of the Reynolds stresses within the boundary layer is much broader for the LES/RANS model. This effect appears to be due to reattachment-shock motion.

7) From a perspective of improving RANS models for this type of flow, it is clear that nominally two-dimensional flow might not be attained downstream of the reattachment line. This means that two-dimensional RANS models must account for the collective effects of pairs of counter-rotating vortices, and it is unclear what average state one might expect to predict. This fact might explain why RANS models, even if tuned to capture the separation-shock location, inevitably fail to capture the correct recovery rate of the boundary layer downstream of reattachment.

Acknowledgments

This work was supported by the U.S. Army Research Office under grant W911NF-06-1-0299, monitored by Thomas Doligalski.

Computer resources were provided by the High-Performance Computing component of North Carolina State University's Information Technologies Division.

References

[1] Dolling, D. S., "Fifty Years of Shock Wave/Boundary-Layer Interaction Research: What Next?," *AIAA Journal*, Vol. 39, No. 8, 2001, pp. 1517–1531.

[2] Marshall, T. A., and Dolling, D. S., "Computation of Turbulent, Separated, Unswept Compression Ramp Interactions," *AIAA Journal*, Vol. 30, No. 8, 1992, pp. 2056–2065.

[3] Dolling, D. S., "High-Speed Turbulent Separated Flows: Consistency of Mathematical Models and Flow Physics," *AIAA Journal*, Vol. 36, No. 5, 1998, pp. 725–732.

[4] McClure, W. B., and Dolling, D. S., "Exploratory Study of Effects of Suction Near Reattachment on the Unsteadiness of a Mach 5 Compression Ramp Interaction," AIAA Paper 91-1767, June 1991.

[5] Gramann, R. A., "Dynamics of Separation and Reattachment in a Mach 5 Unswept Compression Ramp Flow," Ph.D. Dissertation, Dept. of Aerospace Engineering and Engineering Mechanics, Univ. of Texas, Austin, TX, 1989.

[6] Erengil, M. E., and Dolling, D. S., "Separation Shock Motion and Ensemble-Averaged Wall Pressures in a Mach 5 Compression Ramp Interaction," *AIAA Journal*, Vol. 29, No. 5, 1991, pp. 728–735.

[7] Beresh, S. J., Clemens, N. T., and Dolling, D. S., "Relationship Between Upstream Turbulent Boundary-Layer Velocity Fluctuations and Separation Shock Unsteadiness," *AIAA Journal*, Vol. 40, No. 12, 2002, pp. 2412–2422.

[8] Beresh, S. J., Clemens, N. T., Dolling, D. S., and Comninos, M., "Investigation of the Causes of Large-Scale Unsteadiness of Shock-Induced Separated Flow Using Planar Laser Imaging," AIAA Paper 97-0064, Jan., 1997.

[9] Ganapathisubramani, B., Clemens, N. T., and Dolling, D. S., "Effect of Upstream Boundary Layer on Shock-Induced Separation," *Journal of Fluid Mechanics*, Vol. 585, Aug. 2007, pp. 369–394. doi:10.1017/S0022112007006799

[10] Searcy, J. A., "The Effects of Spanwise Structures and Unsteady Forcing of Vortex Generators on Shock Induced Separated Flow using Planar Laser Scattering," M.S. Thesis, Department of Aerospace Engineering and Engineering Mechanics, Univ. of Texas, Austin, TX, 2006.

[11] Ganapathisubramani, B., Clemens, N. T., and Dolling, D. S., "Effect of Upstream Coherent Structures on Low Frequency Motion of Shock-Induced Turbulent Separation," AIAA Paper 2007-1141, Jan. 2007.

[12] Adams, N. A., "Direct Numerical Simulation of Turbulent Compression Ramp Flow," *Theoretical and Computational Fluid Dynamics*, Vol. 12, No. 2, 1998, pp. 109–129. doi:10.1007/s001620050102

[13] Urbin, G., Knight, D., and Zheltovodov, A. A., "Large Eddy Simulation of a Supersonic Boundary Layer Using an Unstructured Grid," *AIAA Journal*, Vol. 29, No. 7, 2001, pp. 1288–1295.

[14] Rizzetta, D. P., Visbal, M. R., and Gaitonde, D. V., "Large-Eddy Simulation of Supersonic Compression-Ramp Flow by High-Order Method," *AIAA Journal*, Vol. 39, No. 12, 2002, pp. 2283–2292.

[15] Rizzetta, D. P., and Visbal, M. R., "Application of Large-Eddy Simulation to Supersonic Compression Ramps," *AIAA Journal*, Vol. 40, No. 8, 2002, pp. 1574–1581.

[16] Loginov, M. S., Adams, N. A., and Zheltovodov, A. A., "Large Eddy Simulation of Shock-Wave/Turbulent-Boundary-Layer Interaction," *Journal of Fluid Mechanics*, Vol. 565, Oct. 2006, pp. 135–169. doi:10.1017/S0022112006000930

[17] Wu, M., and Martin, M. P., "Direct Numerical Simulation of Supersonic Turbulent Boundary Layer over a Compression Ramp," *AIAA Journal*, Vol. 45, No. 4, 2007, pp. 879–889. doi:10.2514/1.27021

[18] Baurle, R. A., Tam, J., Edwards, J. R., and Hassan, H. A., "Hybrid RANS/LES Approach for Cavity Flows: Blending, Algorithm, and Boundary Treatment Issues," *AIAA Journal*, Vol. 41, No. 8, 2003, pp. 1463–1480.

[19] Xiao, X., Edwards, J. R., Hassan, H. A., and Baurle, R. A., "Inflow Boundary Conditions for Hybrid Large-Eddy/Reynolds-Averaged Navier–Stokes Simulations," *AIAA Journal*, Vol. 41, No. 8, 2003, pp. 1481–1490.

[20] Fan, T. C., Edwards, J. R., Hassan, H. A., and Baurle, R. A., "Hybrid Large-Eddy/Reynolds-Averaged Navier–Stokes Simulations of Shock-Separated Flows," *Journal of Spacecraft and Rockets*, Vol. 41, No. 6, 2004, pp. 897–906.

[21] Xiao, X., Edwards, J. R., and Hassan, H. A., "Blending Functions in Hybrid Large-Eddy/Reynolds-Averaged Navier–Stokes Simulations," *AIAA Journal*, Vol. 42, No. 12, 2004, pp. 2508–2515.

[22] Boles, J. A., and Edwards, J. R., "Hybrid Large-Eddy/Reynolds-Averaged Navier–Stokes Simulation of a Mach 8.3 Crossing-Shock Interaction," AIAA Paper 2006-3039, June 2006.

[23] Hunt, D., and Nixon, D., "A Very Large Eddy Simulation of an Unsteady Shock Wave/Turbulent Boundary Layer Interaction," AIAA Paper 95-2122, June 1995.

[24] Roy, C. J., and Edwards, J. R., "Numerical Simulation of a Three-Dimensional Flame/Shock Wave Interaction," *AIAA Journal*, Vol. 38, No. 5, 2000, pp. 745–760.

[25] Edwards, J. R., "A Low-Diffusion Flux-Splitting Scheme for Navier–Stokes Calculations," *Computers and Fluids*, Vol. 26, No. 6, 1997, pp. 635–659. doi:10.1016/S0045-7930(97)00014-5

[26] Colella, P., and Woodward, P. R., "The Piecewise Parabolic Method (PPM) for Gas-Dynamical Simulations," *Journal of Computational Physics*, Vol. 54, No. 1, 1984, pp. 174–201. doi:10.1016/0021-9991(84)90143-8

[27] Menter, F. R., "Two Equation Eddy Viscosity Turbulence Models for Engineering Applications," *AIAA Journal*, Vol. 32, No. 8, 1994, pp. 1598–1605.

[28] Strelets, M., "Detached Eddy Simulation of Massively Separated Flows," AIAA Paper 2001-0879, Jan. 2001.

[29] Walz, A., *Boundary Layers of Flow and Temperature*, MIT Press, Cambridge, MA, 1969 (English translation).

[30] Wilcox, D. C., *Turbulence Modeling for CFD*, 2nd ed., DCW Industries, La Cañada, CA, 1998.

[31] Smits, A. J., and Dussauge, J.-P., *Turbulent Shear Layers in Supersonic Flow*, 2nd ed., Springer, New York, 2006.

[32] Tomioka, S., Jacobsen, L. S., and Schetz, J. A., "Sonic Injection from Diamond-Shaped Orifices into a Supersonic Crossflow," *Journal of Propulsion and Power*, Vol. 19, No. 1, 2003, pp. 104–114.

[33] Wu, M., Bookey, P., Martin, M. P., and Smits, A. J., "Analysis of Shockwave/Turbulent Boundary Layer Interaction Using DNS and Experimental Data," AIAA Paper 2006-6310, Jan. 2005.

[34] Smits, A. J., and Muck, K-C., "Experimental Study of Three Shock-Wave/Turbulent Boundary Layer Interactions," *Journal of Fluid Mechanics*, Vol. 182, Sept. 1987, pp. 291–314. doi:10.1017/S0022112087002349

[35] Zheltovodov, A. A., Schulein, E., and Yakovlev, V. N., "Development of Turbulent Boundary Layers Under Conditions of Mixed Interaction with Shock and Expansion Waves," Inst. of Theoretical and Applied Mechanics, Siberian Branch, Russian Academy of Sciences, Preprint 28-83, Novisobirsk, Russia (in Russian).

[36] Navarro-Martinez, S., and Tutty, O. R., "Numerical Simulation of Görtler Vortices in Hypersonic Compression Ramps," *Computers and Fluids*, Vol. 34, No. 2, 2005, pp. 225–247. doi:10.1016/j.compfluid.2004.05.002

[37] Dussauge, J.-P., Dupont, P., and Debieve, J-F., "Unsteadiness in Shock Wave Boundary Layer Interactions with Separation," *Aerospace Science and Technology*, Vol. 10, No. 2, 2006, pp. 85–91. doi:10.1016/j.ast.2005.09.006

[38] Wu, M., and Martin, M. P., "Analysis of Shock Motion in STBLI Induced Compression Ramp Configuration using DNS Data," AIAA Paper 2007-1136, Jan. 2007.

[39] Settles, G. S., and Dodson, L. J., "Hypersonic Shock/Boundary Layer Interaction Database," NASA CR-177577, Apr. 1991.

[40] Zheltovodov, A. A., Zaulichnii, E. G., Trofimov, V. M., and Yakolev, V. N., "Heat Transfer and Turbulence Study in Compressible Separated Flows," Inst. of Theoretical and Applied Mechanics, Russian Academy of Sciences, Preprint 22-87, Novosobirsk, Russia, 1987.

P. Givi
Associate Editor